# Gravity wave induced instability of the stratospheric polar vortex edge

Lawrence Coy,[a,b] Paul A. Newman,[a] William M. Putman,[a] Steven Pawson,[a] and M. Joan Alexander[c]

[a] *NASA GSFC, Greenbelt, MD, USA*

[b] *SSAI, Lanham, MD, USA*

[c] *NWRA, Boulder, CO, USA*

*Corresponding author*: Lawrence Coy, lawrence.coy@nasa.gov

ABSTRACT: We report on a previously undocumented process capable of mixing Northern Hemisphere (NH) winter Ertel potential vorticity (EPV)—instabilities introduced along the stratospheric polar vortex edge by breaking gravity waves (GWs). As horizontal resolution has increased, global scale atmospheric models and data assimilation systems (DAS) are now able to capture some aspects of GW generation, propagation, and dissipation. This work examines resolved GWs, their breaking, and their interaction with the stratospheric polar vortex as seen in the NASA Global Modeling and Assimilation Office near real time DAS during the 2021–2022 NH winter. This analysis shows that tropospheric generated GWs, breaking in the stratosphere over a substantial area, created a significant disruption of the polar vortex EPV, in turn triggering baroclinic instabilities near the edge of the polar vortex. The instabilities took the form of mini-vortices propagating on the edge of the stratospheric polar vortex that generated mixing signatures. This work revealed two new features in the EPV analysis: high and low fluctuations at the smallest model scale created by resolved GW breaking, and high values associated with mini-vortices along the edge of the polar vortex.

## 1. Introduction

The Northern Hemisphere (NH) stratospheric polar vortex forms every winter, however, considerable vortex variability exists, especially in years with stratospheric sudden warmings (SSWs). During SSW events, high Ertel potential vorticity (EPV) in the stratospheric polar vortex is mixed down to lower latitudes by global-scale planetary waves. The planetary waves are said to be "breaking" when they create regions where the latitudinal EPV gradient is reversed and these reversed gradient regions can lead to instabilities in the wave breaking region (see Butchart 2022, and references therein).

Here we report on another process capable of mixing NH winter EPV—instabilities introduced along the polar vortex edge by breaking gravity waves (GW). GWs are generated by flow over orography, convection, fronts, or flow instabilites (Alexander 2010). Their successful vertical propagation depends on the background atmospheric flow. Under the right conditions GWs can transfer significant momentum and energy from the troposphere to the middle atmosphere. As vertically propagating GWs encounter lower densities or approach a critical layer, they increase in amplitude until they become unstable and "break", depositing momentum and energy to the background flow and hence providing the possibility of disrupting the winter stratospheric polar vortex.

Global scale atmospheric models and data assimilation systems (DAS) routinely resolve the main features of the stratospheric polar vortex and planetary wave variability and breaking. As the horizontal resolution has increased over time these models are now able to capture convective systems and some aspects of GW generation, propagation, and dissipation (Holt et al. 2017; Stevens et al. 2019; Shibuya and Sato 2019). Here we report on resolved GWs, their breaking, and their interaction with the stratospheric polar vortex as seen in the NASA Global Modeling and Assimilation Office (GMAO) near real time forward processing (FP) system during the 2021–2022 NH winter.

Our plan is to examine a somewhat atypical NH winter (2021–2022), where planetary wave activity was relatively weak and the stratospheric polar vortex strong, allowing GWs to dominate the polar vortex disturbances. The working hypothesis is that orographically generated GWs, breaking in the mid-to upper stratosphere, distorted the edge of the polar vortex, creating regions of unstable EPV gradients. These in turn generated a series of what will be called here mini-vortices, incorporating signatures of latitudinal mixing, on the edge of the polar vortex.

In the following, Section 2 provides a description of the DA systems and models used. The main DAS is the NASA GEOS (Global Earth Observing System) FP system, however some lower horizontal resolution MERRA-2 (Modern-Era Retrospective analysis for Research and Applications) output is included for comparison. To investigate the potential for baroclinic instability near the polar vortex edge, results are presented from a linear quasi-geostropic beta plane model, also described in Section 2. The results are presented in Section 3, with subsections on the 2021-2022 NH winter, the resolved GWs, the structure of the mini-vortices, and the linear instability model. A summary of the results along with conclusions are presented in Section 4.

## 2. Global Assimilation Products and Data

### *a. GEOS FP System*

The NASA GMAO GEOS FP DAS routinely produces global, near-real-time, meteorological analysis fields and forecasts available at three hourly intervals. This system updates frequently (approximately every six months) to better incorporate new data types and the latest model developments. The DAS utilizes a full suite of observation types including aerosol, temperature, pressure, radiances, winds, moisture, radio occultation, and ozone measurements. Each six hourly analysis assimilates roughly two million observations. Zhu et al. (2022) provides a current description of the GEOS DAS.

The system used during the NH winter of 2021–2022 was run at 12 km horizontal resolution on a cubed sphere grid (Putman and Lin 2007) with meteorological fields saved on a 5/16 by 1/4 degree longitude by latitude horizontal grid and on either the full 72 model levels (model top at 0.01 hPa) or vertically interpolated to 42 pressure levels. A description of the model physics can be found in Arnold et al. (2020). The most recent two weeks of forecasts are available on the NASA Center for Climate Simulation (NCCS) data portal. The specific archived analysis fields used in the study are available as described in the Open Research Section.

### *b. MERRA-2*

The MERRA-2 system provides ongoing global atmospheric reanalyses starting in 1980. Unlike the FP system, the MERRA-2 system is frozen, with only the input data changing with time. The MERRA-2 vertical levels are the same as in FP, however MERRA-2, with fields saved at 5/8 by 1/2 degree longitude by latitude, has more coarse horizontal resolution than FP. An overview of MERRA-2 is given by Gelaro et al. (2017). Here we used the monthly averaged pressure level fields (GMAO 2015b) when comparing the NH winter 2022 climate with other winters and the instantaneous model level EPV fields (GMAO 2015a) when comparing specific time EPV fields between FP and MERRA-2.

### *c. Linear Instability Model*

The potential for baroclinic instability near the disturbed vortex edge is investigated using a quasi-geostropic, beta-plane, linear instability model. This is the same model used and described in McCormack et al. (2014) and is based on the adiabatic and frictionless, linearized potential vorticity equation (see Andrews et al. 1987, equation 3.4.5 and following equations):

$$q'_t + \overline{u} q'_x + v' \overline{q}_y = 0. \tag{1}$$

where $q$ is potential vorticity, $u$ and $v$ are the longitudinal and meridional velocity components, and $x$, $y$, $t$, are the longitudinal and meridional directions and time. The overbars denote a zonal average and the primes the deviation from a zonal average Since $q'$ and $v'$ depend linearly on the geostropic stream function, $\psi$, assuming a wave solution for $\psi$ with phase speed $c$ and zonal wavenumber $k$ allows the $x$ and $t$ derivatives to be evaluated. With $\overline{u}$ and $\overline{q}_y$ then specified as the environment to be tested for instability, and suitable boundary conditions, Eq. 1 can be finite differenced for a chosen value of $k$ as:

$$\mathbf{A}\psi = c\mathbf{B}\psi \tag{2}$$

where the matrix, $\mathbf{A}$, depends on $\overline{u}$ and $\overline{q}_y$, the matrix, $\mathbf{B}$, depends on the Laplacian operator, and $\psi$ is the vector of stream function values at each point in the two dimensional, latitude and altitude, domain being investigated.

Eq. 2, can be solved for $\psi$ and $c$, using standard routines. For simplicity we assume that the instability is located far enough from the latitude and altitude domain boundaries that we can take $\psi$ equal to zero on all boundaries. Examination of the imaginary part of $c$ allows for the identification of the fastest growing mode structure, $\psi$, for each value of $k$ specified.

### *d. AIRS data*

For confirmation of the DAS resolved GWs we examined the GW signature found in the AIRS (Atmospheric Infrared Sounder on the NASA Aqua satellite) 4.3 $\mu$m brightness temperature signal. Horizontal resolution is 13.5 km at the nadir point below the satellite, similar to the resolution of the FP system, and resolution decreases toward the measurement swath edges so that the average resolution is ~20 km. The data are low-noise multi-channel averages with weighting functions that peak between 30–40 km altitude (Hoffmann et al. 2014). Brightness temperature wave anomalies are attenuated relative to sensible temperature anomalies, with attenuation that is inversely proportional to vertical wavelength. These channels are most sensitive to the longer vertical wavelength ($\geq$15 km) GWs and are not expected to highlight wave breaking regions where the vertical wavelength decreases. Note also that selected AIRS channels are assimilated in the DAS so that the AIRS observations shown here are not entirely independent of the data assimilation output, nevertheless, the AIRS observations shown here can be regarded as an independent analysis of the GWs in the FP system forecasts.

## 3. Results

### *a. The 2021–2022 Northern Hemisphere Winter Stratosphere*

The zonal mean of the zonal wind component at 10 hPa, 60°N provides a useful measure of polar vortex strength that can be used to characterize the NH winter stratosphere. Winters with high seasonally averaged DJF (December, January, February) winds either lack SSWs or have them occurring late in the winter season. The 2021-2022 NH winter had the largest mean seasonal wind seen in the 1980-2023 MERRA-2 time period, with a mean seasonal wind of 46.3 ms$^{-1}$, more than 1.5 standard deviations above the average value of 30.3 ms$^{-1}$.

As with the winds, the planetary-scale wave forcing from the troposphere can be considered over the DJF season and variability is expected depending on interannual tropospheric variability. Here we consider the zonally averaged meridional heat flux at 100 hPa and 60°N as a measure of the wave forcing of the stratosphere. The NH 2021–2022 winter season had the lowest meridional heat flux seen in the 1980-2023 MERRA-2 time period, with a mean seasonal heat flux of 17.2 $\mathrm{Kms^{-1}}$, more than 2 standard deviations below the average value of 24.3 $\mathrm{Kms^{-1}}$. The record low 2021–2022 planetary-scale wave forcing at 100 hPa and 60°N is consistent with the strong stratospheric winds.

The strong winds and low wave forcing conjure up a picture of an undisturbed zonally symmetry polar vortex. Nevertheless, the January 2022 stratospheric polar vortex transformed from a zonally symmetric high Ertel potential vorticity (EPV) configuration (Fig. 1a) on 11 January to a much more disturbed vortex (Fig. 1d) on 27 January. While there is an overall elongation of the 27 January high EPV region, the most striking features are the ragged edge of the vortex (the high EPV region) and the existence of four very high, localized EPV mini-vortices along the polar vortex edge. On 11 January the maximum 850K EPV was ~2,000 PVU while by 27 January the maximum had more than doubled to 4,780 PVU with the highest values associated with the strong EPV mini-vortex at 45°W.

### *b. Resolved gravity waves*

Between 11 and 27 January 2022 small regions of extremely high and low EPV values occurred along the vortex edge, especially over Northern Europe with a maximum value of over 13,000 PVU on 14 January (Fig. 1b). The polar vortex edge distorted in response to these perturbations, creating separation of the high EPV from the main vortex on 14 January from 0°–135°E. By 17 January, the vortex edge became even more distorted as the high and low EPV perturbations continued occurring over Northern Europe (Fig. 1c).

Looking more closely at the 850K EPV on 14 and 17 January (Fig. 2), alternating regions of high and low EPV are seen near the polar vortex edge. The EPV values at these times are as much as 8,000 PVU below and 12,500 PVU above the polar vortex edge value. On the 14th (Fig. 2a) a high EPV feature is seen equatorward and then east of the disturbance region corresponding to the EPV filament identified in Fig. 1b.

That these small-scale EPV disturbances are related to resolved GWs can be seen in the undulations in the height of the 850K potential temperature surface (Fig. 3). The GWs in the height field do not disturb the entire EPV field, as non-dissipating GWs should not be visible in the EPV

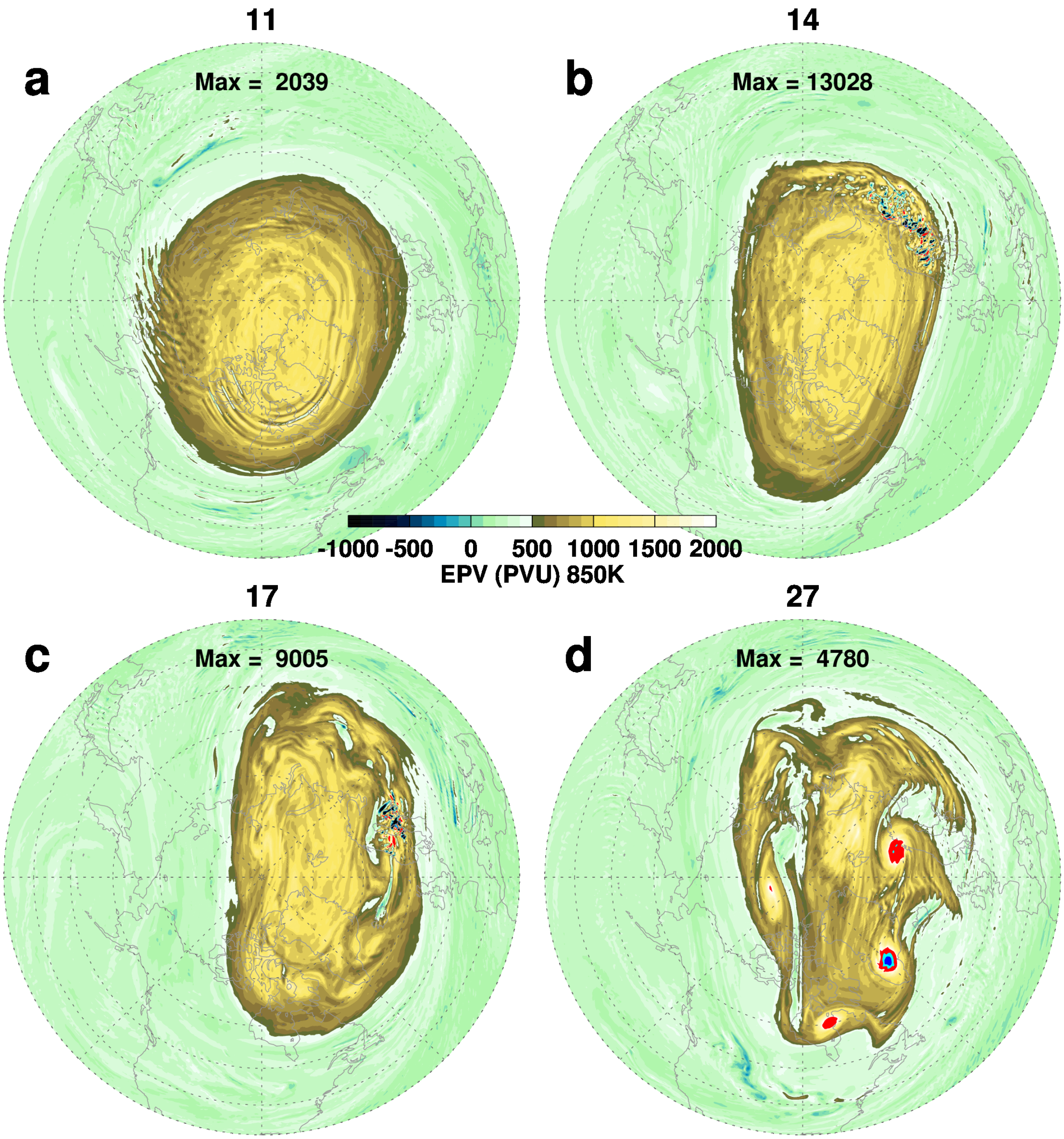


FIG. 1. EPV on the 850K potential temperature surface for a) 11, b) 14, c) 17 and d) 27 January 2022 in potential vorticity units (PVU) where one PVU is equal to $10^{-6} m^2 s^{-1} K kg^{-1}$. The high EPV values are: red: 2000–3000 PVU, cyan: 3000–4000 PVU, blue: 4000–5000 PVU, and yellow: above 5000 PVU.The vortex edge on 11 January 2022 is located at 500 PVU based on the method of Nash et al. (1996).

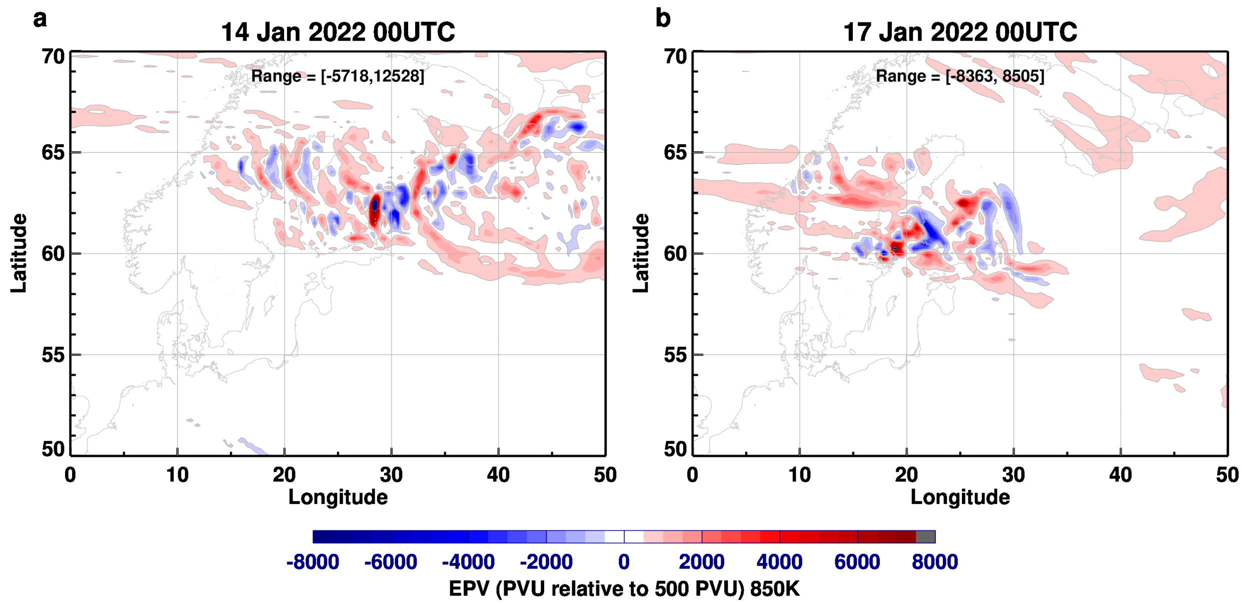


FIG. 2. Latitude (50-70°N) longitude (0°–50°E) projection of EPV on the 850K potential temperature surface for a) 14 January 2022 and b) 17 January 2022. The EPV contours are relative to 500 PVU, the value defining the vortex edge on 11 January 2022.

field, however, the EPV field is disturbed in the more northern part of the GW field where the GWs are likely breaking in a non-EPV conserving manner. Note that the EPV varies on a smaller scale than the scale of the GWs seen in the potential temperature surface oscillations and furthermore that the orientation of the EPV oscillations differs from the orientation of the GWs. This relation between the GW signature and the scale and orientation of the small-scale EPV field is consistent with detailed 3D model studies of GW breaking and with GW observations (Fritts and Alexander 2003, and references therein).

These model resolved GWs can also be seen directly in the AIRS observations (Fig. 4). These wave patterns highlight regions over southern Scandinavia where the strong GWs have the largest vertical wavelengths. Note that these brightness temperatures correspond well with the regions of potential temperature height surface variations shown in Fig. 3. In the regions where EPV fluctuations are large the AIRS GW signal is weak. This is more evidence that the EPV fluctuations characterize regions where GWs are breaking and hence have small vertical wavelengths there.

The vertical cross sections of potential temperature and zonal wind on 14 and 17 January (Fig. 5) highlight the stratospheric breaking wave region, topped by the strong easterly vertical wind shear

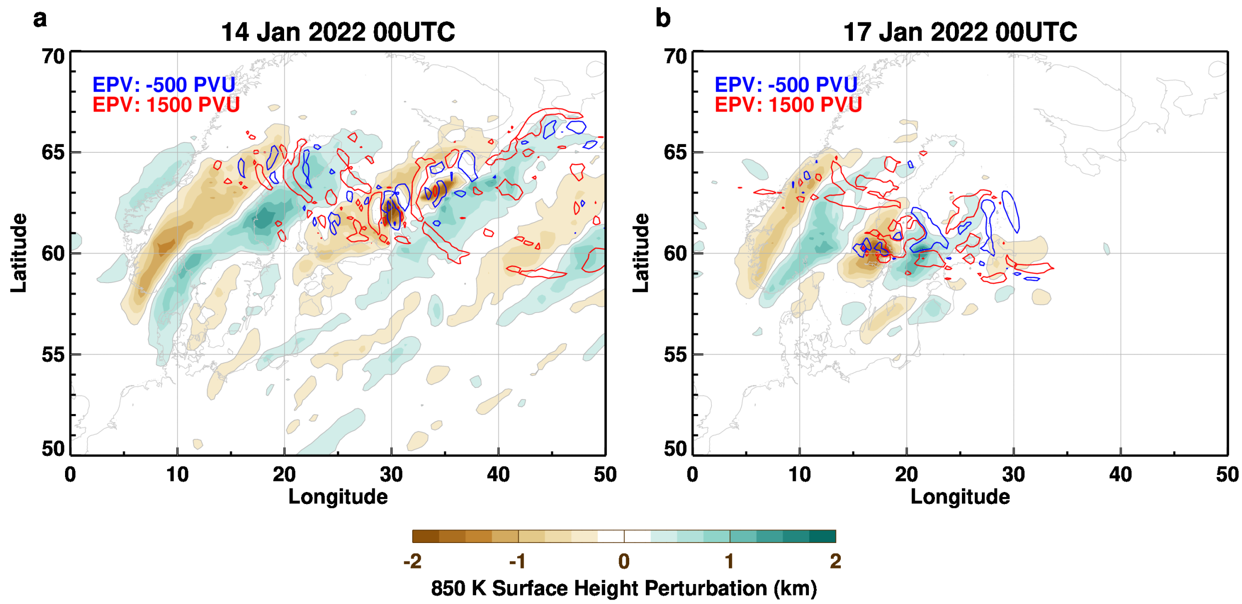


FIG. 3. Latitude (50-70°N) longitude (0°W–50°E) projection of the height of the 850K potential temperature surface (filled contours) and the -500 (blue) and 1500 (red) PVU contours on a) 14 January 2022 and b) 17 January 2022.

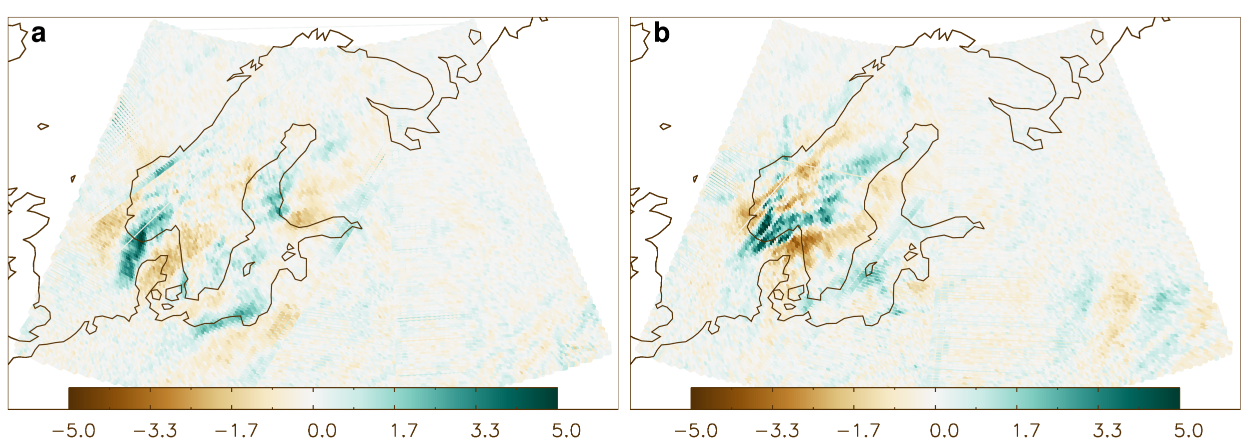


FIG. 4. AIRS 4.3 $\mu$m brightness temperature anomalies on descending (nighttime) overpasses on a) 14 January and b) 17 January showing large amplitude mountain waves over southern Scandinavia. The UT times listed are the overpass times that cover the mountain waves. These are low-noise multi-channel averages described in Hoffmann et al. (2014) with weighting functions that peak between 30–40 km altitude.

and reversal of the zonal wind direction near the stratopause that inhibits the vertical propagation of orographic GWs. Thus the GWs are required to break in the stratosphere at this time. On both

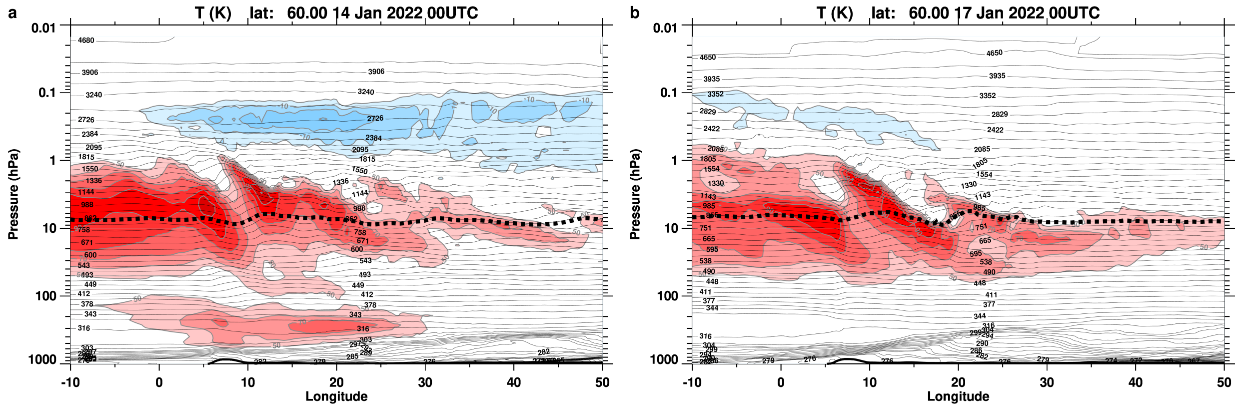


FIG. 5. Longitude (10°W–50°E) altitude (1000–0.01 hPa) cross section at 60°N of potential temperature (gray contours) and zonal wind (filled contours). The dotted black curve denotes the 850K potential temperature surface. The contour interval for the zonal field is 10 $ms^{-1}$ and only winds great than 50 $ms^{-1}$ ( red shades) and less than 0 $ms^{-1}$ (blue shades) are shown.

the 14th and the 17th the strong stratospheric westerlies at 10°W are reduced after crossing the GW region and are much weaker by 50°E, an indication that the wave breaking may be reducing the zonal wind. Nearly vertical potential temperature surfaces are also found on both the 14th and 17th (Fig. 5) indicating breaking gravity waves at 60°N and likely at nearby latitudes as well, including the 60–65°N regions of small scale EPV features seen in Fig. 3.

These relatively large amplitude GWs in the stratosphere were generated by strong tropospheric northwesterly winds over Scandinavia (Fig. 6). The synoptic weather situation at this time was ideal for GW generation with a large, upper-air, high pressure system just west of the European orography. The westerly wind component in both the troposphere and stratosphere allowed wave propagation into the upper stratosphere.

While the 60°N zonal wind during 2021–22 was relatively strong, it did weaken during January 2022, especially over the breaking gravity wave region (Fig. 7a). This weakening of the zonal wind after 11 January corresponds to the time of the peak vertical momentum flux over Europe (Fig. 7b). These strong vertical momentum fluxes are characteristic of GWs. Note that this momentum flux is greatest in the upper stratosphere and weakens above 1 hPa in the mesosphere, consistent with the GW wave structure shown in Fig. 5.

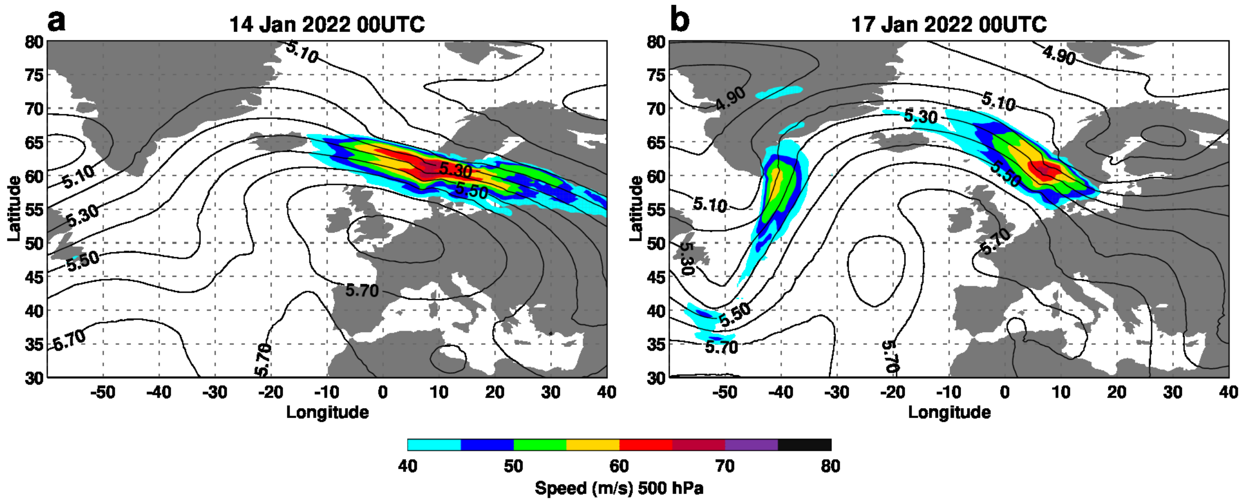


FIG. 6. Wind speed and geopotential heights at 500 hPa for a) 14 January 2022 and b) 17 January 2022.

The small scale GWs and mini-vortices as seen in Fig. 1d can be identified by the occurrence of high values of enstrophy, the square of the vorticity (Fig. 8a). There is a January 2022 burst of enstrophy coincident with the strong vertical momentum flux and these upper stratospheric strong enstrophy values continue to the end of January created by both continued GW activity and the development of the mini-vortices. MERRA-2 lacks the higher horizontal resolution of the NRT system, hence the small scale features seen in the NRT system's enstropy (Fig. 8a) are not seen in MERRA-2 (Fig. 8b). MERRA-2 captures some of the mini-vortices as seen by the slightly high than average enstrophy values during the last third of January at 10 hPa, however, it misses the very strong enstrophy values characteristic of GW breaking near mid-January.

### *c. Mini-Vortices*

The mini-vortices develop and propagate along the edge of the vortex, just poleward of the edge value delineating the low and high EPV regions. An example of the growth and propagation of the mini-vortices from 24–27 January is shown in figure 9. EPV undulations, identified by the letters, A, B, and C can be seen on 24 January (Fig. 9a) in a region of EPV that has separated from the main high EPV region by gravity wave breaking (EPV fluctuations at the smallest resolvable scale) from Greenland to Northern Europe. By 25 January (Fig. 9b), the three mini-vortices have propagated about 90° in longitude around the main vortex. After crossing the main breaking GW region the mini-vortices have increased in amplitude, moving in response to the larger EPV values

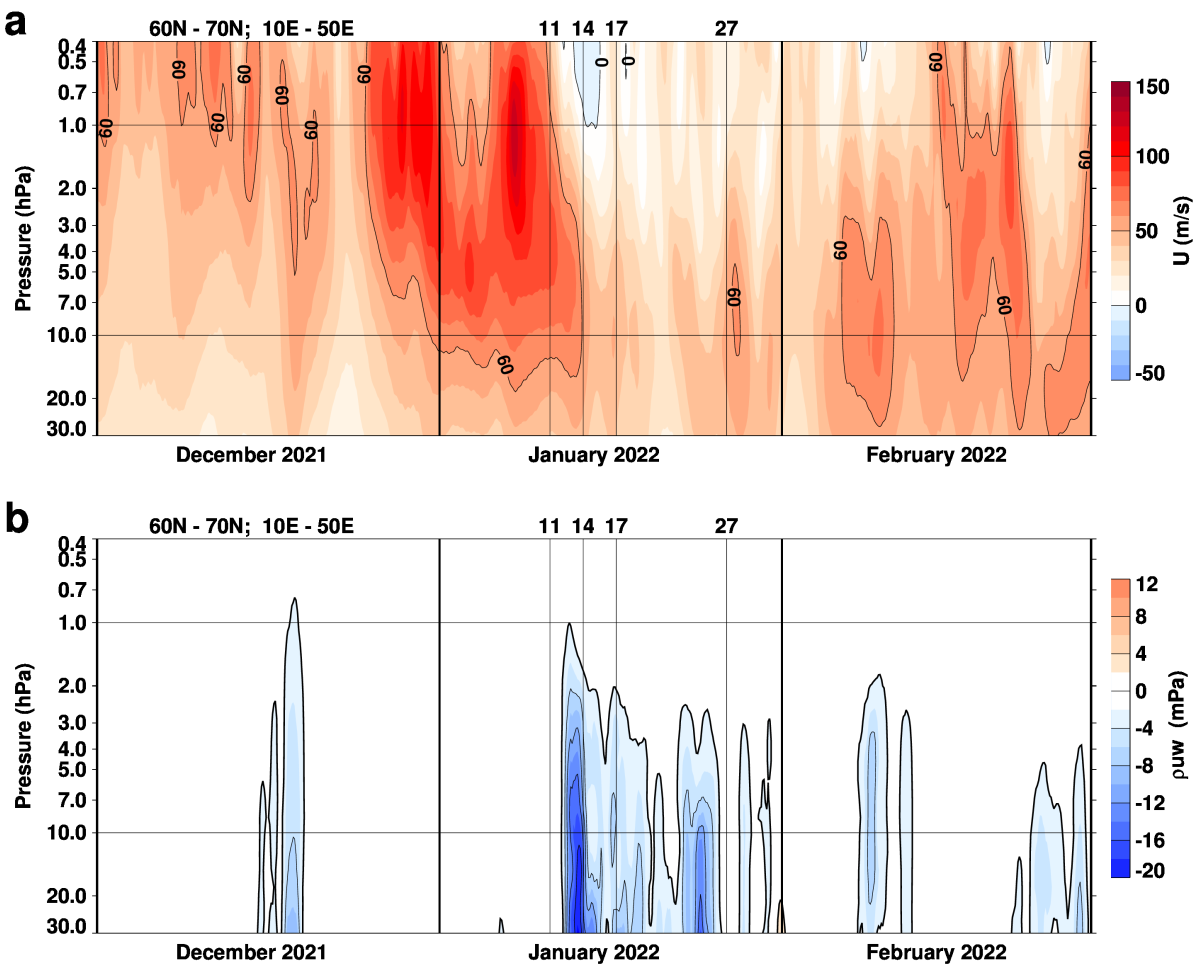


FIG. 7. Time (DJF) pressure (30–10 hPa) cross sections averaged over 60°–70°N and 10°–50°E for a) zonal mean zonal wind (ms$^{-1}$) and b) the zonal component of the density weighted vertical momentum flux (mPa).

of the polar vortex. The mini-vortices, A, B, and C continue to increase in amplitude (the value of their central EPV) on the 26 January (Fig. 9c) and there is also at this time the identification of an additional trailing EPV region labeled D. On the last day shown, 27 January (Fig. 9d), the mini-vortices continue their eastward propagation with A and D increasing in amplitude while B and C decrease slightly in amplitude. Note that some of the mini-vortices are associated with "breaking wave" signatures in the EPV field: A in panel c), and A, B, and C, in panel d). In each of these mini-vortices EPV from the main vortex is being pulled off and lower EPV mixed into the main vortex.

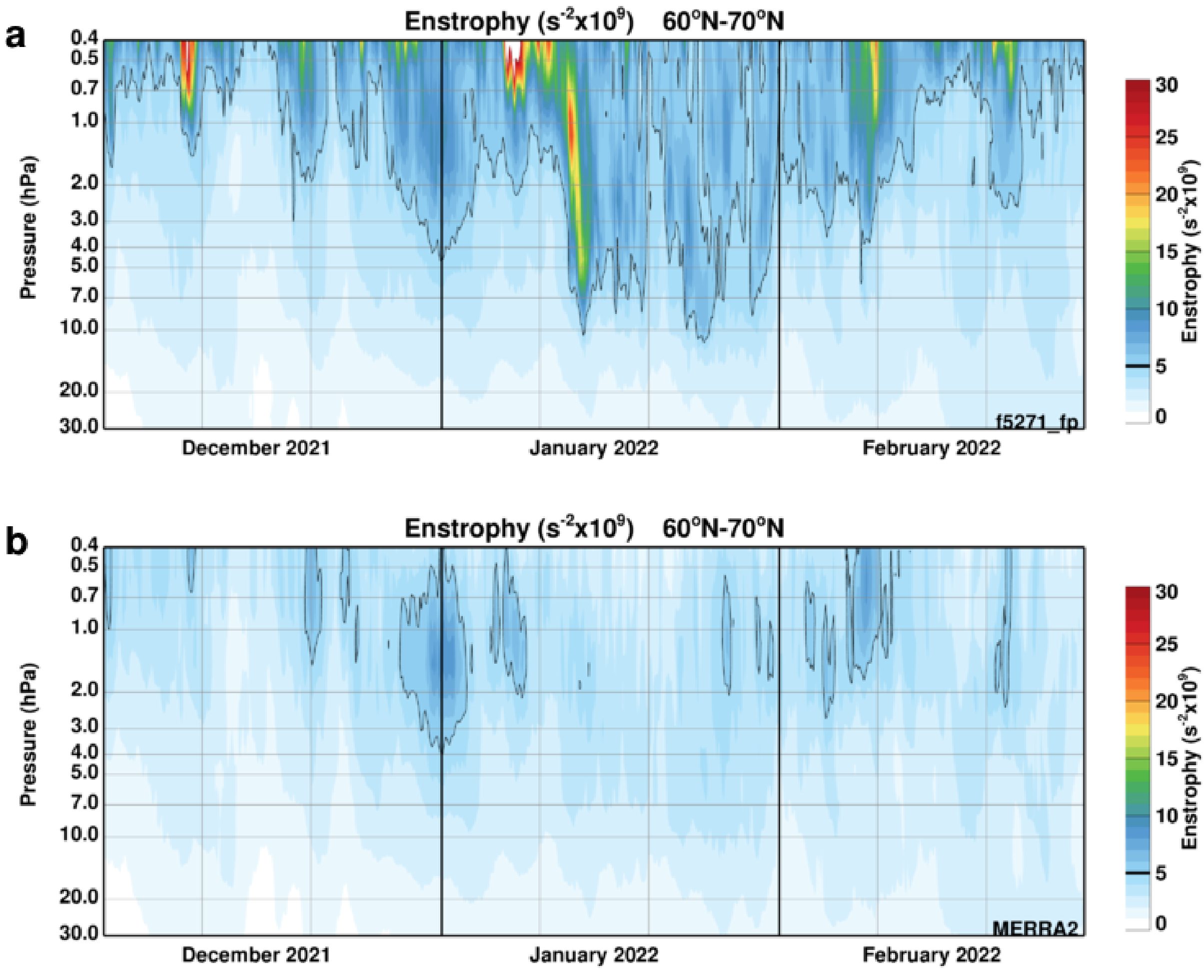


FIG. 8. Time (DJF) pressure (30–10 hPa) zonal averages of enstrophy ($s^{-2} \times 10^6$) over 60–70°N for a) the GMAO NRT system and b) MERRA-2.

The trajectory of the mini-vortex B carried it nearly twice around the main vortex (Fig. 10). After ~2 days increasing in strength (24–26 January) , mini-vortex B kept it's amplitude nearly constant until ~28 January before weakening and crossing over the North Pole on 29 January and eventually dissipating near Northern Europe. Mini-vortex B existed for about seven days making its average period for a circulation around the globe approximately three and half days, implying a propagation speed of 45 $ms^{-1}$ at 70°N.

Cross sections of mini-vortex B on 26 January highlight typical vertical structure of the mini-vortices during their largest amplitude (Fig. 11). The EPV anomaly extends from ~10–1.5 hPa in the upper stratosphere while the potential temperature shows large perturbations starting just

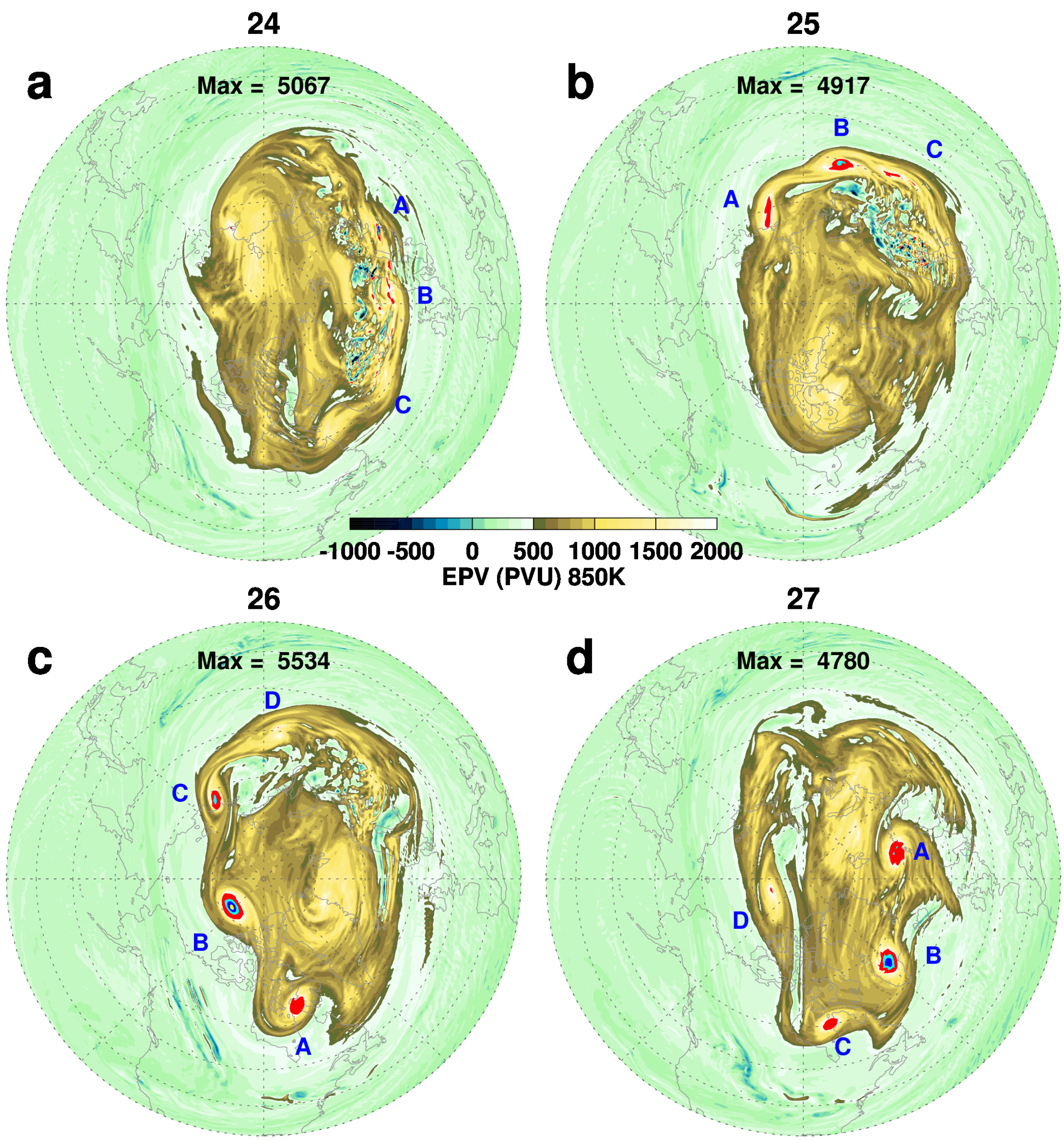


FIG. 9. EPV on 850K potential temperature surface for a) 24, b) 25, c) 26, and d) 27 January 2002 00UTC. The high EPV values are: red: 2000–3000 PVU, cyan: 3000–4000 PVU, blue: 4000–5000 PVU, and yellow: above 5000 PVU. Features tracked across panels are labeled A, B, C, and D.

above 20 hPa and extending through the upper stratosphere. The temperature perturbation field is consistent with the potential temperature field with cool air below and warm air above. The wind

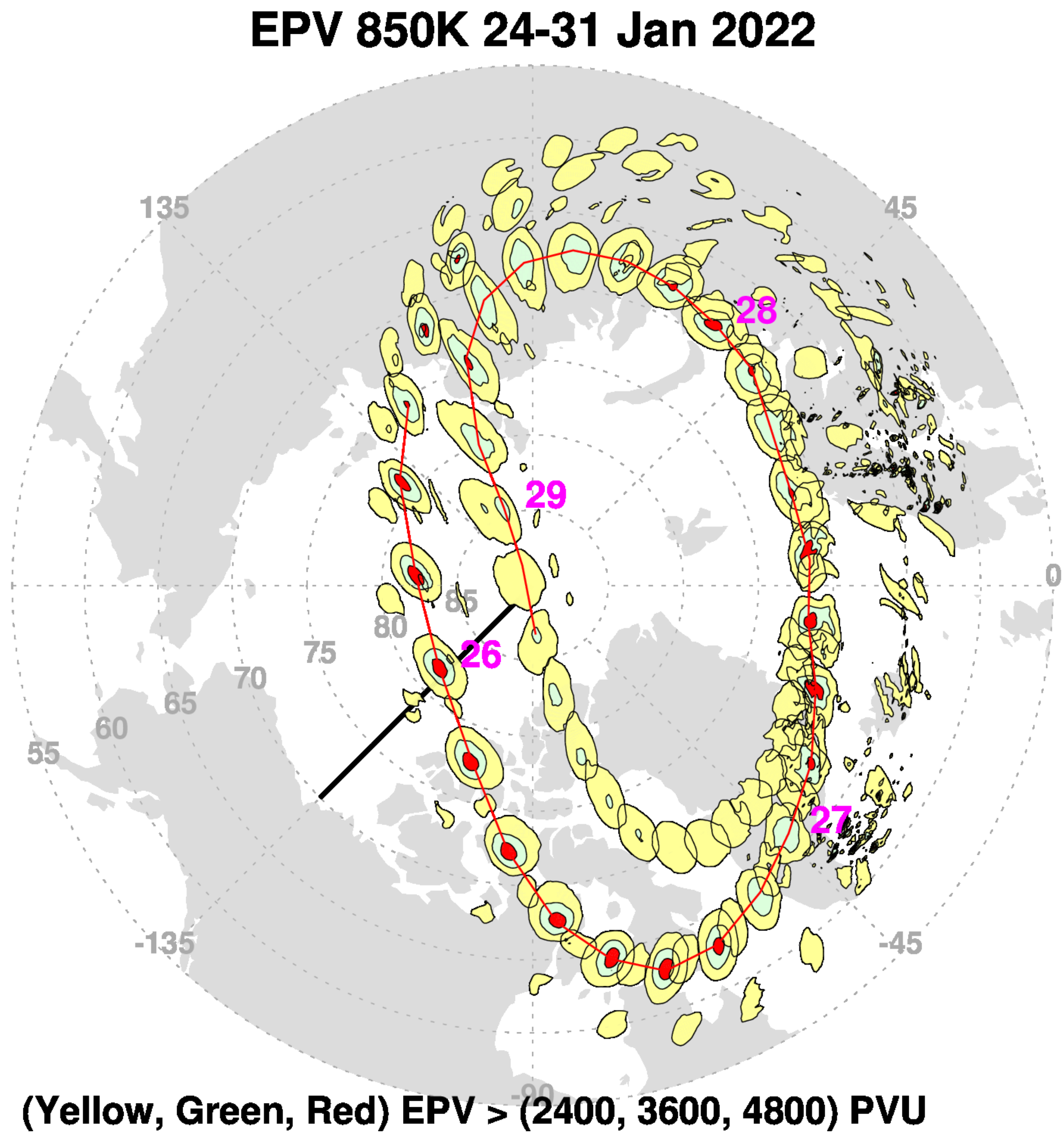


FIG. 10. EPV on the 850K potential temperature surface for 24–31 January 2022 contoured every three hours. EPV values are colored between 2400–3600 PVU (yellow), 3600–4800 PVU (green), and greater than 4800 PVU (red). The red curve connects the maximum EPV locations from 25 January 15 UTC to 29 January 6 UTC. The locations of the highest EPV at 0 UTC on 26, 27, 28, and 29 January are marked. The black line denotes the location of the cross section shown in Fig. 11.

anomalies are located south and north of the axis of the temperature perturbation consistent with the cyclonic circulation of the EPV anomalies. The strongest wind gradients (in the horizontal)

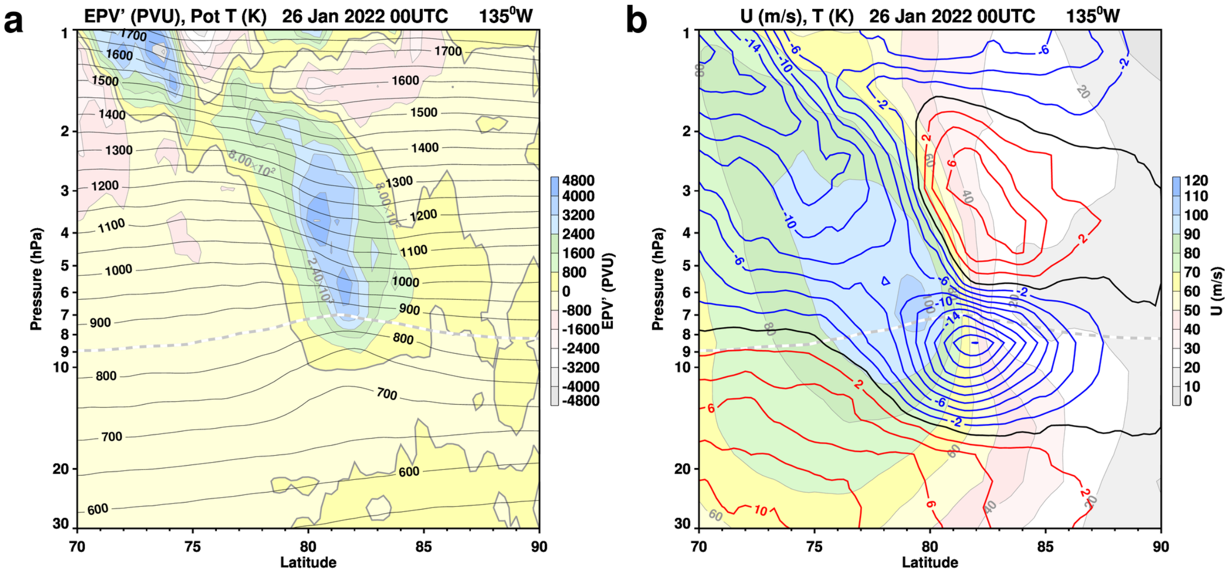


FIG. 11. Latitude (70°–90°N) pressure (30–1 hPa) cross section at 135°W of a) EPV deviation from the zonal mean (PVU, filled contours) and potential temperature (K, black contours) and b) zonal wind (ms$^{-1}$, filled contours) and temperature deviation from the zonal mean (K, red positive, blue negative). The dashed gray curve denotes the 850K potential temperature.

coincide with the strongest temperature gradients (in the vertical). The wind change across the mini-vortex is ~80 ms$^{-1}$. The mini-vortices are located in the upper stratosphere with little extent into the lower stratosphere.

### *d. Instability Considerations.*

The idea presented here is that the tropospheric generated GWs break in the stratosphere over a substantial area, creating a significant disruption of the polar vortex EPV, in turn triggering instabilities near the edge of the polar vortex. The instability then produces the mini-vortices. As a simple test of the instability of the flow, a linear instability model was examine for different zonal wind profiles and times. One result is shown in figure 12. Since the reversed EPV gradient is localized, the zonal winds near the GW activity, 10°–60°E, were average for the background state. The time chosen was for 25 January as the wave perturbation, especially the perturbations labeled C and D in figure 9, were still growing at that time. Other choices include time averaging of the zonal winds or selecting a different longitude range. In addition the model evaluates instability over a limited latitude and pressure range, here chosen to be 58°–68°N and 20–2 hPa. As in

McCormack et al. (2014) the boundary conditions were simply taken to be zero at all boundaries of the box. The interior of the box includes a region of negative $\overline{q}_y$ (Fig. 12a) and a reversal of the EPV gradient (Fig. 12b).

For the above choices the fastest growing unstable wave was found at wavenumber 9, with an e-folding growth rate of 1.4 days, a phase speed of 35 ms$^{-1}$, and a period of 5.5 days. Examining the spacing of the mini-vortex locations of 25 January (Fig. 9b), the wavenumber 9 result is not unrealistic, however the spacing between the mini-vortices does increase with time (Fig. 9d) suggesting a smaller wavenumber. The growth rate is reasonable, however the phase speed appears to be somewhat slow, leading to a period that is longer than observed when compared to the just over 3-day circuit of the globe taken by the mini-vortex B (Fig. 9) from 26–29 January (Fig. 10). The amplitude structure is confined to the lower region of the model's domain in contrast to the larger vertical extent seen in figure 11. Overall, the instability model results, while not comprehensive, illustrate the potential for instability created by the breaking GW induced reversal in the local EPV latitudinal gradient.

## 4. Summary and Conclusions

This study based on the 12 km resolution DAS revealed two new features in the EPV analysis: high and low fluctuations at the smallest model scale created by resolved GW breaking, and high values associated with mini-vortices along the edge of the polar vortex. In this case both types of anomalous EPV values were related, as the persistent GW breaking created a region of reversed EPV gradient that triggered the formation of the mini-vortices.

The location of NH maximum and minimum values of 850K EPV at each analysis time provides a convenient overview of the breaking GW regions during January 2022 (Fig. 13). During the first ten-days the highest EPV values are at the highest latitudes and lowest EPV values are at the lower latitudes, consistent with the NH climatological poleward gradient of EPV. By the middle of January, however, the distribution has changed with maximum and minimum EPV locations close together over Northern Europe, the Greenland coast, and Iceland. These indicate regions of strong GW breaking as seen in the EPV field. Later in January, these "salt and pepper" patterns continue with the addition of several days (25–29 January) when the maximum EPV value was associated with a propagating mini-vortex.

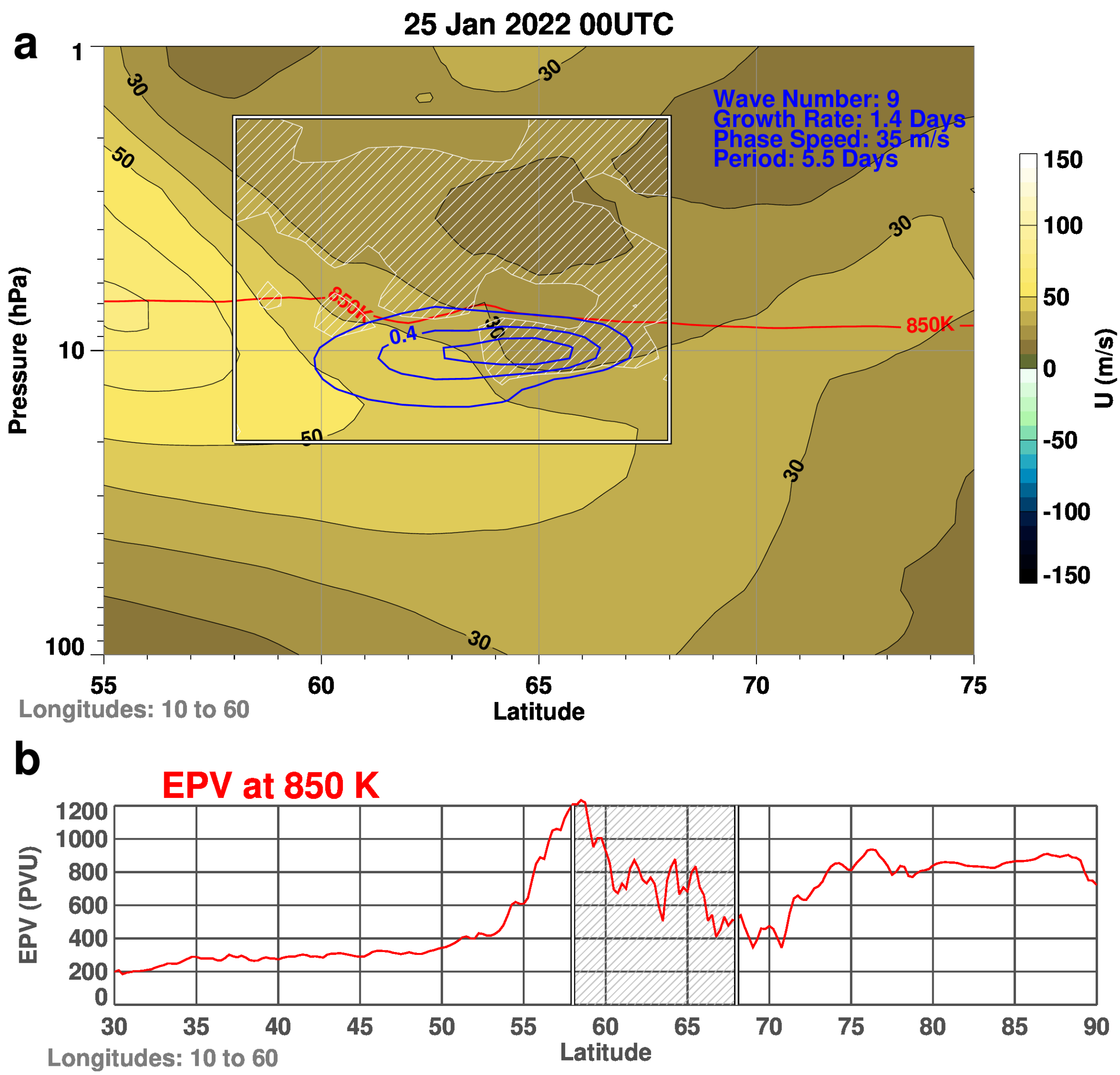


292 Fig. 12. a) zonal mean wind averaged over 10–60°$E$ (filled contours), the region of negative $\overline{q}_y$ (shaded), the 850K potential temperature (red contour), the non-dimensional fastest gowing wave amplitude (blue contours), and b) EPV (PVU) averaged over 10–60°$E$ as a function of latitude. The box in a) and the shaded region in b) denotes the stability model domain used

The maximum value of 850K EPV can characterized the overall NH winter of 2021–22 with a nominal maximum value of just under 2000 PVU for most of the winter season (Fig. 14). Starting on 14 January values that are 5× higher appear, coincident with the appearance of GW breaking. These spikes continue for the remainder of the month with the addition of a more consistent in time

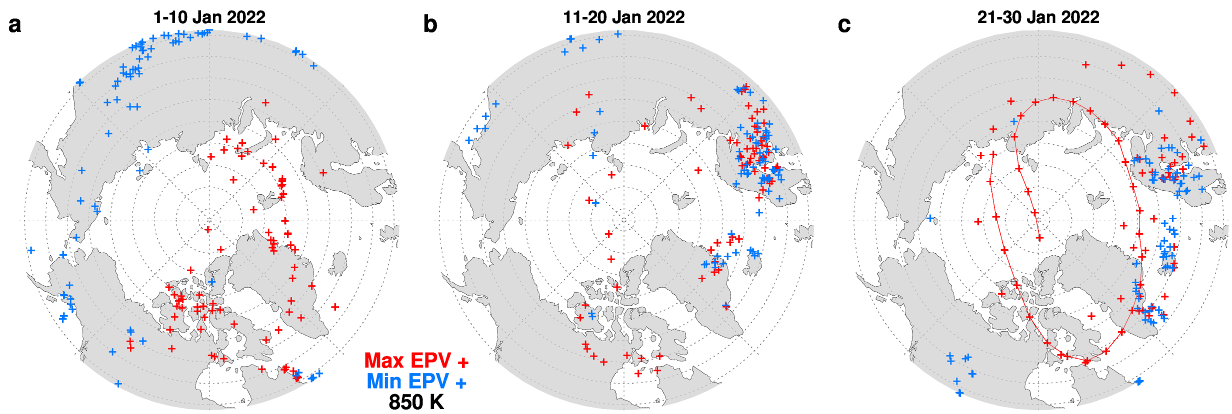


FIG. 13. The locations of the maximum (red) and minimum (blue) values of EPV on the 850K potential temperature surface at each analysis time for a) 1–10, b) 11–20, and c) 21–30 January 2022. The minimum locations are restricted to the area shown on the map projection. The red curve connects the maximum EPV locations from 25 January 15 UTC to 29 January 9 UTC.

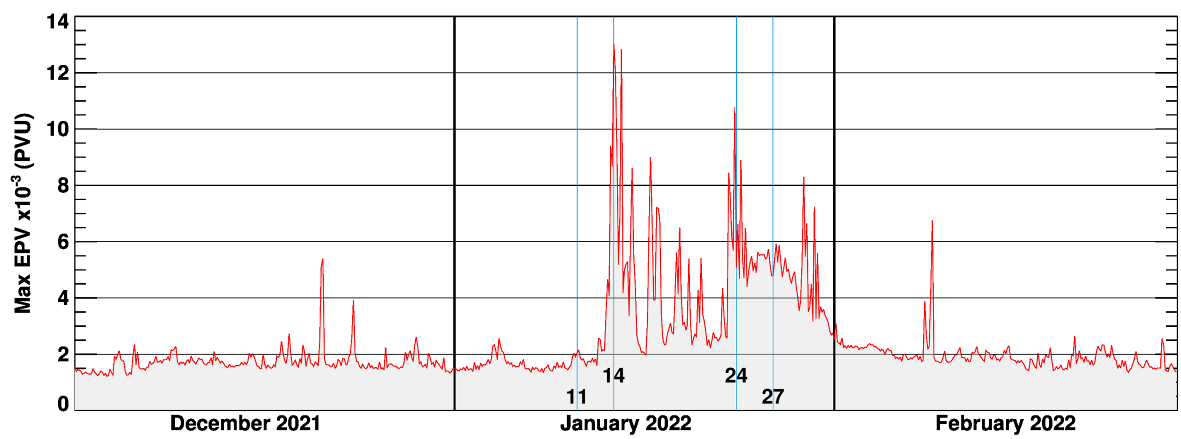


FIG. 14. Maximum EPV value on the 850K potential temperature surface as a function of time ($10^{-3}$ PVU). 11, 14, 24, and 27 January 2022 are denoted by blue vertical lines.

bulge of high EPV, a signature of the persistent mini-vortices. These dramatic events are mostly over by the start of February.

How realistic are these very high EPV values seen in DAS? It is difficult to be definitive at this time. Comparison of the evolution of the mini-vortices in FP (Fig. 9) with the lower resolution MERRA-2 EPV fields (Fig. 15) shows that at lower resolution the FP mini-vortices can still be identified as a smoothed version of the higher resolution system. If the wind change is approximately the same across a mini-vortex but the doubled horizontal resolution allows for a doubling of the gradient, then the EPV values can be expected to double as well. Note that the MERRA-2 system is unable to capture the smallest scale EPV fluctuations in the breaking GW region.

The different orientation and scale of EPV fluctuations from that of the associated GWs needs further investigation. Detailed three dimensional models of GW breaking (Fritts et al. 2009a,b) resolve the small scale, rapid, variability created during the breaking process and the generation of EPV by breaking GWs has been recently modeled by Waite and Richardson (2023). These studies suggest that "spanwise", that is disturbances along the wavefront, commonly develop, however relating these to global scale EPV is not yet clear.

While we have focused on a single NH winter in which planetary wave activity was relatively weak to highlight the GWs and their effects on the polar vortex, it is likely that breaking GWs in the mid to upper stratosphere are fairly common and routinely contribute to mixing at the edge of the polar vortex. In future studies we plan to examine other years when high resolution FP DAS fields are available and develop algorithms to search for the weaker signals of these stratospheric polar mini-vortices in the longer time record of the lower resolution MERRA-2 DAS.

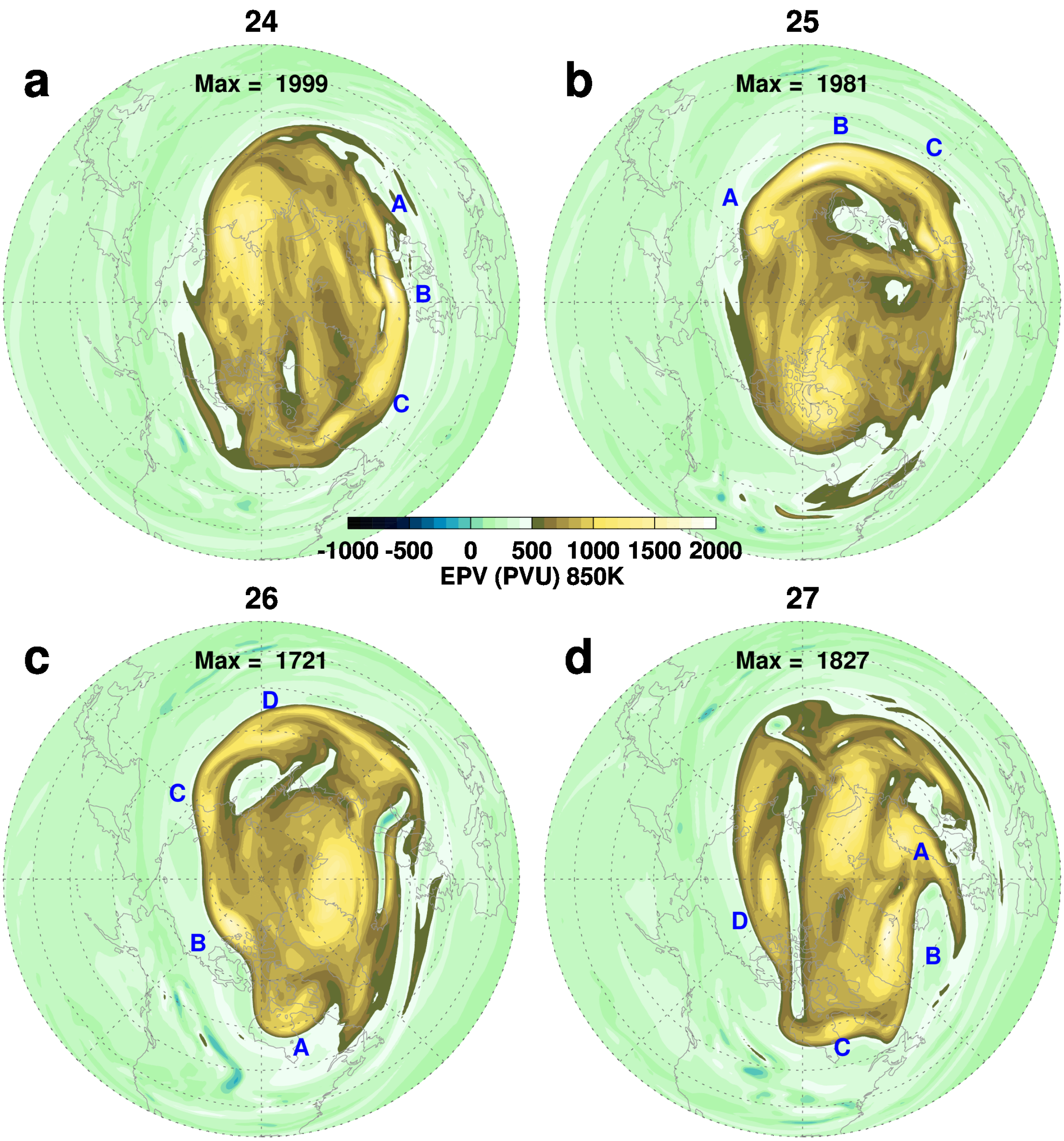


330 FIG. 15. EPV on 850K potential temperature surface for a) 24, b) 25, c) 26, and d) 27 January 2002 00UTC.
331 As in Fig. 9 but for MERRA-2.

*Acknowledgments.* his work was supported by NASA MAP (Grant NNG17HP01C) and ACMAP programs (Grants 80NSSC19K1005, NNH18ZDA001N). Resources supporting this work were provided by the NASA High-End Computing (HEC) Program through the NASA Center for Climate Simulation (NCCS) at Goddard Space Flight Center.

*Data availability statement.* The GEOS data used in this study/project have been provided by the Global Modeling and Assimilation Office (GMAO) at NASA Goddard Space Flight Center. The Forward Processing (FP) DAS output are archived at `https://portal.nccs.nasa.gov/datashare/gmao/geos-fp/das` and the system used in this study is labeled f5271_fp. The MERRA-2 data is available from the NASA's Goddard Earth Sciences Data and Information Services Center (GES DISC, https://disc.gsfc.nasa.gov/datasets?project=MERRA-2). Specific MERRA-2 data sets used are contained in the references. The AIRS brightness temperatures are available from `https://datapub.fz-juelich.de/slcs/airs/gravity_waves/html/view_2022_014.html` The IDL (Interactive Data Language) code used for the quasi-geostrophic instability model is archived at `https://gmao.gsfc.nasa.gov/gmaoftp/larrycoy/instability_code/stability_package.pro`.

## References

Alexander, M. J., 2010: Gravity waves in the stratosphere. *The Stratosphere: Dynamics, Transport, and Chemistry*, L. M. Polvani, A. H. Sobel, and D. W. Waugh, Eds., American Geophysical Union, Washington, DC, 109–122.

Andrews, D. G., J. R. Holton, and C. B. Leovy, 1987: *Middle Atmosphere Dynamics*. Academic Press, 489 pp.

Arnold, N. P., W. M. Putman, and S. R. Freitas, 2020: Impact of resolution and parameterized convection on the diurnal cycle of precipitation in a global nonhydrostatic model. *Journal of the Meteorological Society of Japan. Ser. II*, **98 (6)**, 1279–1304, https://doi.org/10.2151/jmsj.2020-066.

Butchart, N., 2022: The stratosphere: a review of the dynamics and variability. *Weather and Climate Dynamics*, **3 (4)**, 1237–1272, https://doi.org/10.5194/wcd-3-1237-2022, URL https://wcd.copernicus.org/articles/3/1237/2022/.

Fritts, D. C., and M. J. Alexander, 2003: Gravity wave dynamics and effects in the middle atmosphere. *Reviews of Geophysics*, **41 (1)**, https://doi.org/https://doi.org/10.1029/2001RG000106, URL https://agupubs.onlinelibrary.wiley.com/doi/abs/10.1029/2001RG000106, https://agupubs.onlinelibrary.wiley.com/doi/pdf/10.1029/2001RG000106.

Fritts, D. C., L. Wang, J. Werne, T. Lund, and K. Wan, 2009a: Gravity wave instability dynamics at high reynolds numbers. part i: Wave field evolution at large amplitudes and high frequencies. *Journal of the Atmospheric Sciences*, **66 (5)**, 1126 – 1148, https://doi.org/https://doi.org/10.1175/2008JAS2726.1, URL https://journals.ametsoc.org/view/journals/atsc/66/5/2008jas2726.1.xml.

Fritts, D. C., L. Wang, J. Werne, T. Lund, and K. Wan, 2009b: Gravity wave instability dynamics at high reynolds numbers. part ii: Turbulence evolution, structure, and anisotropy. *Journal of the Atmospheric Sciences*, **66 (5)**, 1149 – 1171, https://doi.org/https://doi.org/10.1175/2008JAS2727.1, URL https://journals.ametsoc.org/view/journals/atsc/66/5/2008jas2727.1.xml.

Gelaro, R., and Coauthors, 2017: The Modern-Era Retrospective Analysis for Research and Applications, Version 2 (MERRA-2). *Journal of Climate*, **30 (14)**, 5419–5454, https://doi.org/10.1175/JCLI-D-16-0758.1, URL https://doi.org/10.1175/JCLI-D-16-0758.1, https://doi.org/10.1175/JCLI-D-16-0758.1.

GMAO, 2015a: Global Modeling and Assimilation Office, inst3 3d asm Nv: MERRA-2 3D Assimilated Meteorological Fields 3-hourly (model level, 0.625x0.5L42), version 5.12.4. Greenbelt, MD, USA: Goddard Space Flight Center Distributed Active Archive Center (GSFC DAAC), accessed June 2016, https://doi.org/10.5067/WWQSXQ8IVFW8.

GMAO, 2015b: Global Modeling and Assimilation Office, instM 3d asm Np: MERRA-2 3D IAU State, Meteorology Monthly Averaged 3-hourly (p-coord, 0.625x0.5L42), version 5.12.4. Greenbelt, MD, USA: Goddard Space Flight Center Distributed Active Archive Center (GSFC DAAC), accessed June 2016, https://doi.org/10.5067/2E096JV59PK7.

Hoffmann, L., M. J. Alexander, C. Clerbaux, A. W. Grimsdell, C. I. Meyer, T. Rößler, and B. Tournier, 2014: Intercomparison of stratospheric gravity wave observations with AIRS and IASI. *Atmospheric Measurement Techniques*, **7 (12)**, 4517–4537, https://doi.org/10.5194/amt-7-4517-2014, URL https://amt.copernicus.org/articles/7/4517/2014/.

Holt, L. A., M. J. Alexander, L. Coy, C. Liu, A. Molod, W. Putman, and S. Pawson, 2017: An evaluation of gravity waves and gravity wave sources in the southern hemisphere in a 7 km global climate simulation. *Quarterly Journal of the Royal Meteorological Society*, **143 (707)**, 2481–2495, https://doi.org/https://doi.org/10.1002/qj.3101, URL https://rmets.onlinelibrary.wiley.com/doi/abs/10.1002/qj.3101, https://rmets.onlinelibrary.wiley.com/doi/pdf/10.1002/qj.3101.

McCormack, J. P., L. Coy, and W. Singer, 2014: Intraseasonal and interannual variability of the quasi 2 day wave in the northern hemisphere summer mesosphere. *Journal of Geophysical Research: Atmospheres*, **119 (6)**, 2928–2946, https://doi.org/https://doi.org/10.1002/2013JD020199, URL https://agupubs.onlinelibrary.wiley.com/doi/abs/10.1002/2013JD020199, https://agupubs.onlinelibrary.wiley.com/doi/pdf/10.1002/2013JD020199.

Nash, E. R., P. A. Newman, J. E. Rosenfield, and M. R. Schoeberl, 1996: An objective determination of the polar vortex using ertel's potential vorticity. *Journal of Geophysical Research: Atmospheres*, **101 (D5)**, 9471–9478, https://doi.org/https://doi.org/10.1029/96JD00066, URL https://agupubs.onlinelibrary.wiley.com/doi/abs/10.1029/96JD00066, https://agupubs.onlinelibrary.wiley.com/doi/pdf/10.1029/96JD00066.

Putman, W. M., and S.-J. Lin, 2007: Finite-volume transport on various cubed-sphere grids. *Journal of Computational Physics*, **227 (1)**, 55–78, https://doi.org/https://doi.org/10.1016/j.jcp.2007.07.022, URL https://www.sciencedirect.com/science/article/pii/S0021999107003105.

Shibuya, R., and K. Sato, 2019: A study of the dynamical characteristics of inertia–gravity waves in the antarctic mesosphere combining the PANSY radar and a non-hydrostatic general circulation model. *Atmospheric Chemistry and Physics*, **19 (5)**, 3395–3415, https://doi.org/10.5194/acp-19-3395-2019, URL https://acp.copernicus.org/articles/19/3395/2019/.

Stevens, B., and Coauthors, 2019: DYAMOND: the DYnamics of the Atmospheric general circulation Modeled On Non-hydrostatic Domains. *Prog Earth Planet Sci*, **6 (61)**, URL https://doi.org/10.1186/s40645-019-0304-z.

Waite, M. L., and N. Richardson, 2023: Potential vorticity generation in breaking gravity waves. *Atmosphere*, **14 (5)**, https://doi.org/10.3390/atmos14050881, URL https://www.mdpi.com/2073-4433/14/5/881.

Zhu, Y., R. Todling, and N. Arnold, 2022: Observation impact and information retention in the lower troposphere of the gmao geos data assimilation system. *Monthly Weather Review*, **150 (8)**, 2187 – 2205, https://doi.org/https://doi.org/10.1175/MWR-D-21-0334.1, URL https://journals.ametsoc.org/view/journals/mwre/150/8/MWR-D-21-0334.1.xml.